Quenching of initial ac susceptibility in single-domain Ni nanobars

Zheng Gai,* X.-G. Zhang, Ivan I. Kravchenko, Scott T. Retterer, and J. F. Wendelken
Center for Nanophase Materials Sciences, Oak Ridge National Laboratory, Oak Ridge, Tennessee 37831, USA
(Received 19 August 2011; revised manuscript received 28 November 2011; published 3 January 2012)

The ac susceptibility measurement probes the dynamic properties of a magnetic material, which is believed to consist of magnetization rotation and domain wall motion contributions. Here we report the observation of a complete quenching of the initial ac susceptibility for a single-domain Ni nanobar array, when the ac field is aligned with the long axis of the bars. The vanishing of the susceptibility in one direction is a unique nanoscale phenomena, allowing an unambiguous determination of the magnetic state of the nanostructure and a clean separation of different contributions to its dynamic properties. For example, an unambiguous determination of the temperature-dependent surface anisotropy energy is obtained when the field is applied perpendicular to the long axis, even when the size of the nanobar is still large and the surface anisotropy does not dominate the magnetic energy.

DOI: 10.1103/PhysRevB.85.024401 PACS number(s): 75.75.−c, 75.78.−n, 75.60.−d, 81.07.−b

I. INTRODUCTION

Magnetic properties of materials anchor the magnetic recording and nonvolatile memory technologies.[1,2] Performance optimization has pushed device dimensions smaller and thinner, rapidly reaching the nanoscale, where many novel and often unexpected properties begin to emerge. Such dramatic changes in the properties of the materials can either benefit or harm device performance. For example, some out-of-plane magnetized nanostructures may transform to in-plane magnetization when their size or temperature is changed.[3] This phenomenon, called the spin reorientation transition (SRT), is caused by the change in the relative size or even sign of the different contributions to the magnetic anisotropy energy, whose different parts scale differently with the dimension of the material. Emerging nanoscale phenomena are often the consequence of several competing factors, e.g., the competition between bulk and surface anisotropy in the case of SRT. Other than theoretical calculations,[4] the experimental determination of the surface anisotropy energy was basically by estimating from the thickness of the SRT of the system.[5]

Recently, a low-field complex ac susceptibility measurement successfully revealed the detailed dynamic domain wall motion modes of ultrathin magnetic films.[6] In pure nickel film, the peak in the temperature dependence of the initial ac susceptibility corresponding to the ferromagnetic phase transition has a tail that extends well into the low-temperature range. Later, it was reported that this long tail follows a surprising power-law scaling with temperature.[7,8] This result raises new questions about the relative significance of the contributions to the low-field susceptibility from domain wall motion and from moment rotation. There has not been any experiment where either of these contributions has been completely removed so that the other contribution can be studied without any ambiguity.

Scaling to the nanoscale makes it possible to achieve a clean separation of different contributions. In particular, sufficiently small magnetic nanodots are single domain, removing any contribution to the susceptibility from domain wall motion. Furthermore, because of the large surface-to-bulk ratio, shape anisotropy becomes dominant in nanostructures, so that by engineering the geometric shape of the nanodots, the moment orientation can be precisely controlled, at least within a certain temperature range.

Here we report low-field ac susceptibility measurements on single-domain, geometrically engineered Ni nanostructure (Ni nanobars) arrays, and compare the results with measurements on arrays containing multidomain nanostructures. At high temperatures (between 170 K and room temperature), the initial ac susceptibility along the length of the nanobars for single-domain samples is completely quenched, in sharp contrast to the multidomain samples which yield results in agreement with the scaling-law behavior reported previously.[7,8] In other words, for single-domain nanobars along the length of the bar there is neither a domain wall motion contribution to the susceptibility, as expected, nor is there any contribution from moment rotation, leading to the conclusion that the moment is "frozen" along this direction. Clear identification of this magnetic state allows the unambiguous determination of the surface anisotropy energy through the measurement along directions perpendicular to this axis. Below 170 K, a spin reorientation transition is observed.

II. EXPERIMENTAL METHODS

The arrays of nickel nanobars were manufactured on Si(100) wafer using e-beam lithography. A positive e-beam resist, ZEP 520A (Zeon Corp.) was spin coated onto oxygen-plasma-cleaned Si wafers and then soft baked for 2 min on a 180 °C hot plate. The resulting photoresist films were approximately 300 nm thick. The exposures were performed on a JEOL-9300FS electron beam lithography tool at an acceleration voltage of 100 kV and beam current of 2 nA. Completed patterns were developed in xylenes for 40 s, rinsed with isopropanol, and blow dried with nitrogen gas. The wafers were descummed in oxygen plasma at 100 W for 6 s using a Technics reactive ion etching (RIE) system. The resulting samples were coated with a Ni film in an e-beam physical vapor deposition (PVD) system. To avoid unnecessary background signals during magnetic measurements no adhesion layers such as thin Cr or Ti metallic films were used. Because nickel (111) surface has the lowest energy, the nanobar is mainly (111) textured polycrystalline.[9] Following the deposition step,

sonication of the wafers in an acetone bath for 2.5 min removed the unexposed resist that resulted in a successful lift-off transfer of the exposed patterns onto the Si surface. Defect-free patterns covering sample areas as large as 7.3 × 9.6 millimeters have been reliably reproduced on a number of wafers. Due to the proximity effect during the e-beam lithography process the width of the Ni structures is about 40% larger than designed value.

Magnetic force microscopy (MFM) images were taken using a Veeco AFM with a NSC14/Co-Cr/50 noncontact silicon cantilever. The ac and dc magnetization were measured using a Quantum Design magnetic properties measurement system (MPMS-XL) with field up to 7 T. Special care was necessary during mounting of the samples because of their fragile nature and the very small signals from the samples. The sample surfaces were never touched during the handling and measurements. The samples were demagnetized and the magnet was reset by quenching the superconducting solenoid and compensating for remnant fields before all the ac measurements. The ac measurements were conducted with 10 Hz (all the data shown in this paper) and 100 Hz under an ac field of 1 Oe and zero dc field. ac susceptibilities measured at different frequencies are essentially the same.

III. RESULTS AND DISCUSSION

Experimental research on magnetic nanostructures has been performed, in general, on large assemblies of particles.[1,2,10,11] The dispersion of morphologies, compositions, orientations, and separations of the magnetic entities have limited the interpretation of the results. To simplify the parameters, we chose laboratory-fabricated arrays of Ni nanobars with identical aspect ratios, separations, and compositions. The thickness of the nanobars can be varied to tune the magnetic properties, creating for example single magnetic domains or multidomains. Figure 1(a) shows typical scanning microscopy (SEM) images of the nanobar arrays manufactured on Si(100) using e-beam lithography. Defect-free patterns covered whole sample areas. As shown in the schematic drawing in Fig. 1(b), the Ni nanobars were rectangular, high aspect ratio bars with a nominal width of 70 nm and 1 micron in length. To minimize the possible dipolar interactions among the bars, MFM images of bar arrays with different distances were systematically studied. The bars used in this paper were arranged on an orthogonal grid pattern with a pitch of 0.5 microns and 1.5 microns in the X and Y directions, respectively. As shown in the MFM images (Fig. 2) from different thickness samples, the magnetic domains from the neighboring nanobars are uncorrelated to each other, indicating that the bar-bar dipolar interaction is not strong enough to influence the magnetic domain configuration. For all the samples we studied, bars with thickness of 15 nm and 30 nm show single magnetic domains [Fig. 2(b), bright contrast at one end and dark contrast at the other end of the bars], while all the 70 nm thick nanobars and the 50 nm films show multiple magnetic domains [Fig. 2(d), alternate bright and dark contrast on the bars]. The arrays of 50 nm thick nanobars show the combination of single and multiple magnetic domains.

The ac and dc magnetizations were measured using MPMS-XL (7T).[10,11] All the samples were measured with magnetic field polar (out-of-plane), longitudinal parallel (in-plane, along the long axis), and longitudinal perpendicular (in-plane, along the short axis) to the nanobars [see the schematic drawing in Fig. 1(b)]. For comparison, the ac susceptibility χ and dc magnetization curves are normalized by the thickness a of the nanobars.

A. Nanobars with multiple magnetic domains

The low-field initial ac susceptibilities χ of multiple magnetic domain bars are very similar to the χ of Ni films.[7] Shown in Fig. 3(a) are the temperature-dependent initial ac susceptibilities of $a = 70$ nm bars measured with the applied magnetic field in three different directions, longitudinal parallel, longitudinal perpendicular, and polar to the sample surfaces. The susceptibility in the parallel

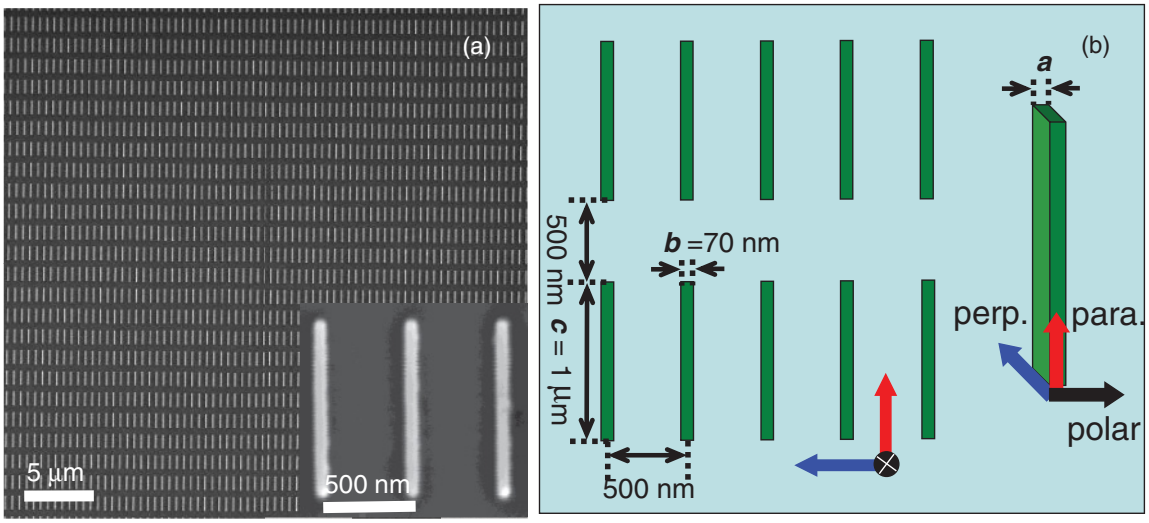

FIG. 1. (Color online) (a) Typical SEM images of the Ni nanobar arrays; inset shows the details of three bars. (b) Schematic drawing of the geometry of the nanobars (a, b, c) and the magnetic field direction notations used in the paper, longitudinal parallel (para.), longitudinal perpendicular (perp.), and polar (polar).

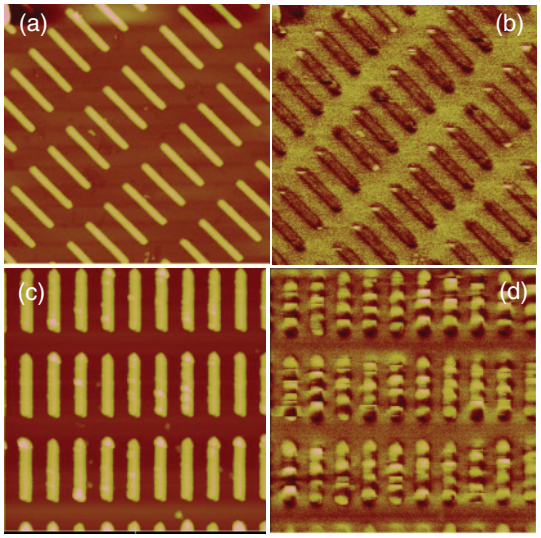

FIG. 2. (Color online) AFM and the corresponding MFM images (5 μm × 5 μm) of nanobar arrays with thickness of (a), (b) 15 nm and (c), (d) 70 nm. MFM image (b) shows single magnetic domains, while (d) shows multidomains. During imaging, the stray field of the magnetic tip can flip the domains of the nanobars, which is reflected in the MFM images as sudden jumps between scanning lines.

direction increases dramatically with increasing temperature, whereas the temperature dependence is much weaker in the other two directions. Using the same normalization as Song *et al.*[7] the susceptibility data of the nanobars for the parallel direction fall on the same universal scaling curve for the films as their Fig. 5, confirming the validity of the low-temperature scaling law in the multiple magnetic domain nanobars.

dc hysteresis loops are essential to help understand the above ac susceptibility behavior. As shown in Fig. 3(b), the 2 K dc loop in the polar direction shows almost full remanence and coercivity, which indicates a strong out-of-plane easy axis. The RT dc loops [Fig. 3(c)] show neither significant remanence nor coercivity in both polar and parallel directions, which normally indicates the existence of a temperature induced out-of-plane to in-plane spin reorientation transition. However, the monotonically increased ac susceptibility and the out-of-plane magnetic domains in the RT MFM image, Fig. 2(d), strongly indicate that the out-of-plane easy axis is maintained up to RT. The similar counterintuitive magnetization of Ni films was quantitatively studied and carefully addressed previously by the magnetization of domain walls,[12,13] which we believe also validates its occurrence in the nanobars. By combining the literature results[12,13] and both MFM images and dc magnetization loops, the most plausible magnetic domain model is schematically drawn in Fig. 3. The magnetic domain configuration of the Ni bars is perpendicular domains with Bloch domain walls, which are capped with canted closure domains on the surface. The number of domain walls in the perpendicular direction of the bars should be zero because of the small width *(b)* of the bars [Fig. 2(d)]. Such a configuration makes the polar and perpendicular directions similar, in contrast to the two in-plane directions and one out-of-plane direction for a film geometry.

When magnetizing the bars along the polar direction, the polar magnetization is a combination of short-range Bloch domain wall motion processes and the closure magnetization rotation. The in-plane magnetization (perp. and para.) is dominated by the long-range rearrangement of Bloch domain walls and the magnetization rotation of the out-of-plane domains and the canted closure domains.[12] Although all the RT hysteresis loops show no remanence and coercivity, they show very different magnetization behaviors as marked by the black arrows in Fig. 3(c). The magnetization process (increasing field) along the polar direction involves the growing of domains

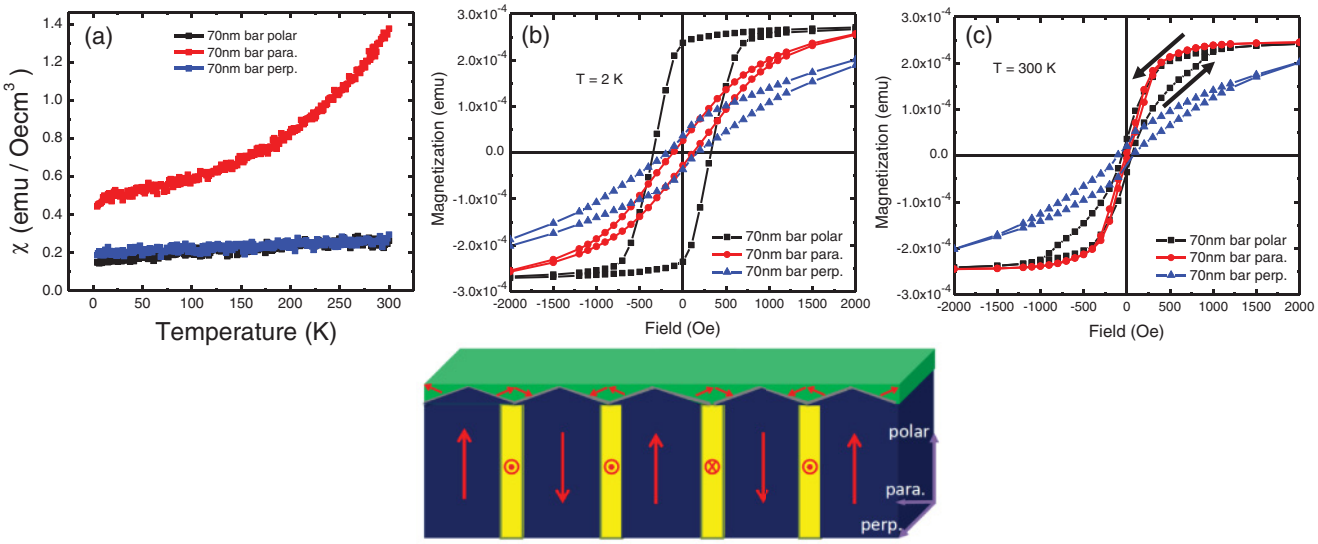

FIG. 3. (Color online) Temperature dependence of the ac susceptibilities (a) and magnetic hysteresis loops [(b) at 2 K and (c) at 300 K] of arrays of 70 nm nanobars (a = 70 nm), measured with the magnetic field applied longitudinal parallel, longitudinal perpendicular, and polar to the sample surfaces. The schematic drawing shows the out-of-plane magnetization configuration of the bars, which consists of the out-of-plane domains (blue), the Bloch domain walls (yellow), and the canted closure domains (green).

along the field and shrinking of the domains opposite the field, thus requiring domain wall motion. In contrast, the magnetization process in the parallel direction only involves moment rotation due to the dipolar coupling created by the parallel field between the out-of-plane domains. Thus the former process needs more energy than the latter, yielding a slower rise of the moment with the applied field (black curve for increasing field). In contrast, the curves for decreasing fields reflect thermally activated magnetization relaxation process, which is similar for both directions. It is not surprising then that the two curves almost coincide for decreasing fields. At RT, although a large polar field can move the Bloch domain walls, the walls recover through thermal activation when the field is removed, leading to zero remanence and coercivity. At 2 K, domain wall energy becomes too large to be overcome by thermal energy, leading to a nearly full remanence.

The ac susceptibilities in the three directions can be readily understood with the above magnetic domain configuration. The ac susceptibility is the rate of change of the magnetization of a material in response to an applied magnetic field. The higher energy required for Bloch domain wall motion when field is applied in the polar direction results in a correspondingly small low-field ac susceptibility.[7,12] The weak temperature dependence of the polar χ indicates that the domain wall motion is not thermally activated at low field. The perpendicular direction for nanobars is more difficult to magnetize than the parallel direction due to the shape anisotropy of the elongated geometry.

The larger values of ac susceptibility χ in the parallel direction than in the other two directions arises from the fact that the magnetization rotation of the out-of-plane domains along the parallel direction, which as we discussed earlier makes up the contribution to the parallel χ, is much easier than domain wall motion (needed for the polar χ) or magnetization rotation along the perpendicular direction (needed for the perpendicular χ). Because in the parallel direction the magnetization rotations of different domains are correlated due to the long-range dipolar interaction, a situation quite similar to thin films, it is not surprising that the χ scales with the temperature with the same scaling law as in thin films.[7]

B. Nanobars with a single magnetic domain

The ac susceptibilities of single-domain bars show very different behavior than the films and multidomain bars. Shown in Fig. 4 are the summarized data of χ for $a = 15$ nm, 30 nm, 50 nm, and 70 nm bars. In both parallel and perpendicular directions, the temperature dependence of χ is nonmonotonic for single-domain bars in sharp contrast to the monotonic increase for 70 nm multidomain bars.

The most striking result for single-domain bars is the quenching of the ac susceptibility above about 170 K up to room temperature in the parallel direction in which the external field is applied along the long axis of the nanobars in Fig. 4(a). In this temperature range, the susceptibility decreases to zero within the sensitivity of the equipment. In the vicinity of 170 K, the average susceptibility is 0.02 emu/Oe cm^3, compared to the equipment sensitivity of 0.05 emu/Oe cm^3. The quenching of the ac susceptibility χ remains almost complete all the way up to room temperature, only increasing slightly to 0.09 emu/Oe cm^3 at 300 K.

The measured susceptibility is also quite unusual in the perpendicular direction in which the external field is applied along the short axis of the bar, Fig. 4(b). Unlike for the multidomain nanobars where χ is almost constant at a small value for the whole temperature range, χ changes dramatically with the temperature for single-domain nanobars. At high temperatures, χ appears to be almost thickness independent. A distinct peak in χ is observed around 130 K for single-domain samples but not for multidomain samples. At the low-temperature end all curves seem to converge to about the same value, and within the same range as χ for the parallel direction.

The ac susceptibilities of $a = 15$ nm bars (Fig. 4) share nonmonotonic trends in both directions similar to but stronger than those in the 30 nm bars, with a higher peak height in the medium-temperature range and a smaller susceptibility at the low-temperature end.

The unusual features of χ are not due to the existence of other phases such as those observed in antiferromagnetic NiO. The oxidation of Ni bars is negligible since NiO normally shows very large coercivities and loop shifts ($\geqslant$10 KOe),[14]

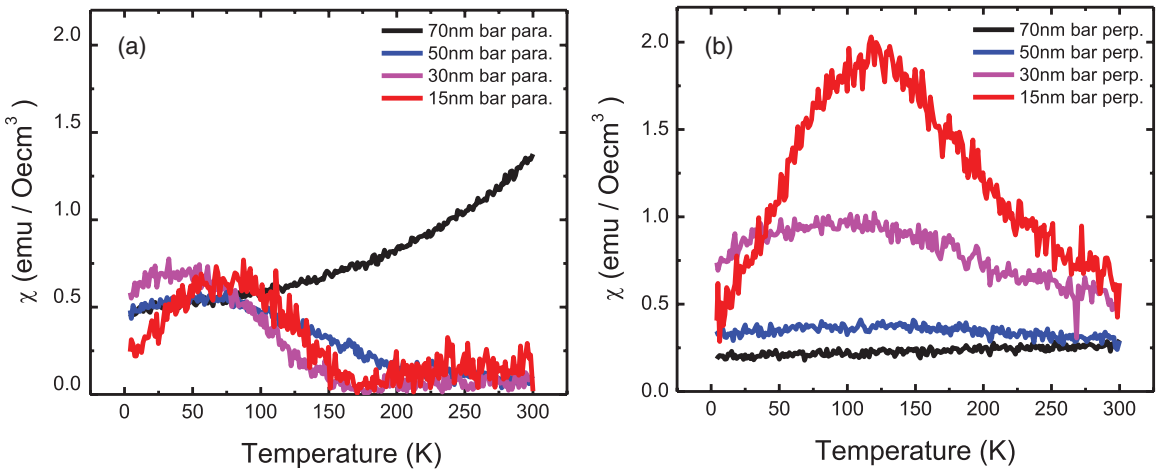

FIG. 4. (Color online) Temperature dependence of the ac susceptibilities of nanobars ($a = 70$, 50, 30, and 15 nm) measured with the magnetic field applied (a) longitudinal parallel and (b) longitudinal perpendicular.

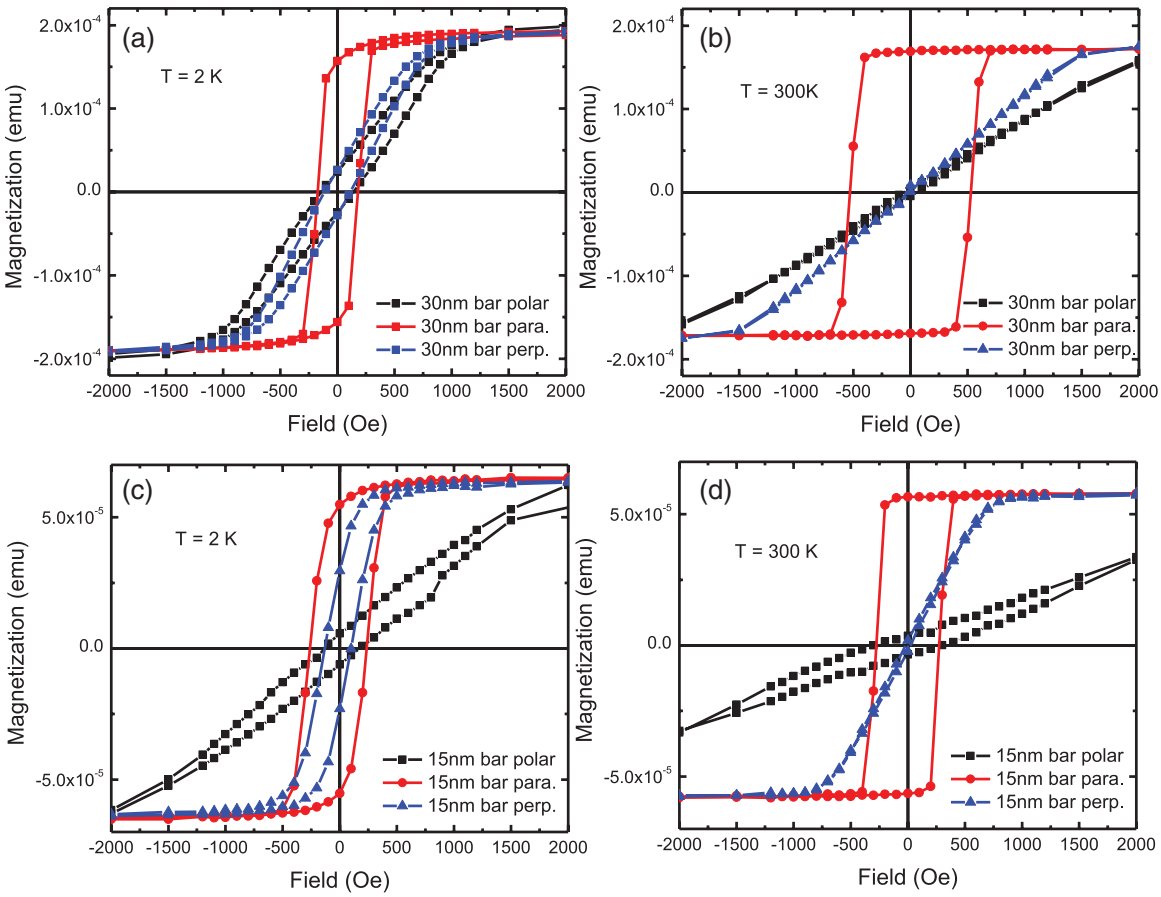

FIG. 5. (Color online) Magnetic hysteresis loops of arrays of 30 nm and 15 nm nanobars ($a = 30$ nm, 15 nm) (a), (c) at 2 K and (b), (d) at 300 K measured with the magnetic field applied longitudinal parallel, longitudinal perpendicular, and polar to the sample surfaces.

which were never observed in our Ni samples—freshly fabricated or old, films or nanobars.

The dc magnetic hysteresis loops for $a = 30$ nm and $a = 15$ nm single-domain bars are shown in Fig. 5. At RT in the parallel direction, Figs. 5(b) and 5(d), both samples have full remanence and large coercivity, indicating this as the easy axis. The preference for the easy-axis direction is not so clear at low temperatures [Figs. 5(a) and 5(c)]. The polar direction is the hardest axis over the whole temperature range compared to the perpendicular direction. It is interesting to compare to the hysteresis loops for 70 nm bars [Figs. 3(b) and 3(c)]. Contrary to the multiple magnetic domain bars, the easy-axis preference of the single-domain bars is stronger at room temperature than at low temperature. We will see in the analysis later that this is due to a spin reorientation transition in the single-domain bars around 130 K.

C. Understanding the ac susceptibility

The peak in the temperature dependence of the ac susceptibility for the single-domain nanobars near 130 K can be understood as the signature of a spin reorientation transition. However, at higher temperatures the quenching of the susceptibility along the parallel direction and the nearly thickness-independent susceptibility along the perpendicular directions call for a further analysis.

To understand the physics underlying the complicated ac susceptibilities of the single magnetic domain bars, it is necessary to recall the energy terms involved in the system. For a low-dimensional magnetic system, the energy terms might include spontaneous-magnetization-related exchange energy, magnetocrystalline anisotropy controlled by the crystalline structure of the system, stress-induced magnetoelastic anisotropy, magnetostatic anisotropy or the demagnetizing energy caused by the shape of the system, surface anisotropy resulting from the broken symmetry of the system, and Zeeman energy.[15–17]

For a simple phenomenological model, it would help to extract only the part that makes the difference. For the multiple and single magnetic domain bars in the current study, the main difference is the thickness of the bars (above 50 nm or below). This means that the main energy terms involved in changing the ac susceptibility behavior are the magnetostatic anisotropy (shape anisotropy) and the surface anisotropy. In the following calculation, the sum of these two anisotropies is expressed as E_s. The sum of the rest of the anisotropy energies that are independent of the geometry of the nanobars is called the bulk anisotropy energy E_b. Then the total energy of the nanobars can be written as $E = E_b + E_s$.

The bulk anisotropy energy per unit volume for a cubic lattice is in the form

$$E_b = K_1\left(m_1^2m_2^2 + m_2^2m_3^2 + m_3^2m_1^2\right) + K_2m_1^2m_2^2m_3^2, \qquad (1)$$

where m_1, m_2, and m_3 are the components of $\mathbf{m}$ along three crystallographic axes.

The expressions of E_s are very different for nanobars with multiple or single magnetic domains because of the existence of magnetic domain walls. In this analysis we focus our interest on the single magnetic domain case. For nanobars with single magnetic domains, the lowest order shape anisotropy and surface anisotropy can be written as a surface integral,

$$E_s = \frac{1}{2}K_s \int (\mathbf{m}\cdot\mathbf{n})^2 dS, \tag{2}$$

where $\mathbf{m}$ is the unit vector along the direction of the magnetic moment and $\mathbf{n}$ is the unit vector along the normal of the surface. For a nanobar, if it favors the moment orientation along the direction with the longest dimension then it implies that $K_s > 0$.

Neglecting the thermal excitation of the magnetic moment, which is negligible for sufficiently large moments, the orientation of the moment is at the minimum of the total energy F per unit volume under an external magnetic field,

$$F(\theta,\phi) = E(\theta,\phi) - M_s H\cos\theta, \tag{3}$$

where M_s is the saturation moment per unit volume and H is the magnetic field; θ and ϕ are the usual polar coordinates. Under this approximation, the temperature dependence of the moment orientation arises from the temperature dependence of the coefficients K_S, K_1, and K_2 in the anisotropy energy.

1. Longitudinal parallel direction

Let us first consider the magnetic moment and susceptibility for a field along the longitudinal parallel direction of the nanobars. For sufficiently large H, the minimum is at $\theta = 0$, i.e., the direction along the magnetic field. For this case, $\partial M/\partial H \approx 0$. Additional minima exist if H is less than a saturation field H_s by minimizing Eq. (3) with respect to θ and ϕ.

Here we list two possible minima and the corresponding values of $F(\theta,\phi)$ that we are interested in. All the other possible minima are listed in the Appendix.

Case 1, for $\sin\theta = 0$, which only is a minimum if $K_s > 0$,

$$F(\theta,\phi) = F_1 = -M_s H. \tag{4}$$

This minimum does not have a corresponding saturation field, and the initial susceptibility

$$\partial M/\partial H \approx 0. \tag{5}$$

Case 3, for $\sin\phi = 0$ and (for small H)

$$\cos\theta \approx -\frac{M_s H}{2K_s\left(\frac{1}{a}-\frac{1}{c}\right)+\frac{4}{3}K_1+\frac{7}{9}K_2}, \tag{6}$$

where a, b, c are the dimensions of the bar along the x, y, z directions, respectively, and $a < b < c$. This is a minimum if $2K_s(1/a - 1/c) + 4K_1/3 + 7K_2/9 < 0$. The saturation field is

$$H_s = -\frac{2K_s\left(\frac{1}{a}-\frac{1}{c}\right)-K_1+\frac{1}{6}K_2}{M_s}, \tag{7}$$

and the initial susceptibility,

$$\frac{\partial M}{\partial H} \approx \frac{M_s^2}{\frac{7}{3}K_1 - \frac{11}{18}K_2 - H_s M_s}. \tag{8}$$

2. Longitudinal perpendicular direction

Similarly, we can calculate the moment and the susceptibility for a longitudinal field perpendicular to the bar (along the b direction). Please note that for this calculation the coordinate system is rotated so that a is along y, b is along z, and c is along x.

Again, we list the two possible minima corresponding to those in the parallel direction; the other minima are included in the Appendix.

Case 1′, we have $\sin\phi = 0$ and

$$\cos\theta = \frac{M_s H bc}{2K_s(c-b)}. \tag{9}$$

The saturation field is

$$H_s = \frac{2K_s(c-b)}{M_s bc}, \tag{10}$$

and the initial susceptibility is

$$\frac{\partial M}{\partial H} = \frac{M_s^2 bc}{2K_s(c-b)}. \tag{11}$$

Case 3′ is $\cos\phi = 0$ and

$$\cos\theta \approx -\frac{M_s H}{2K_s\left(\frac{1}{a}-\frac{1}{b}\right)+\frac{4}{3}K_1+\frac{7}{9}K_2}. \tag{12}$$

The saturation field is

$$H_s = -\frac{2K_s\left(\frac{1}{a}-\frac{1}{b}\right)-K_1+\frac{1}{6}K_2}{M_s}, \tag{13}$$

and the initial susceptibility is

$$\frac{\partial M}{\partial H} \approx \frac{M_s^2}{\frac{7}{3}K_1 - \frac{11}{18}K_2 - H_s M_s}. \tag{14}$$

If $a \ll b$ then the initial susceptibilities along the b and c directions are essentially the same. Consequently the values for $\cos\theta$ and the initial susceptibility are both the same as in case 3 of the longitudinal parallel direction.

The initial susceptibility data, including the unusual quenching of the single-domain nanobars, can be explained nicely by the above simple theory if at the high-temperature range the system is in cases 1 and 1′ and at low temperature it falls in cases 3 and 3′. Note that there is an energy barrier between the low-field state and the high-field state so that the hysteresis cannot be predicted by small-field theory.

At the high-temperature end, in the parallel direction, as predicted by the theoretical calculation in case 1 [Eq. (5)], the ac susceptibilities for single-domain bars are all near 0 [Fig. 4(a)], i.e., a complete quenching of the χ. The few percent of deviation from zero in the experimental data is from the thermal activation effect; the higher the temperature, the larger the deviation is. In the perpendicular direction, as shown in

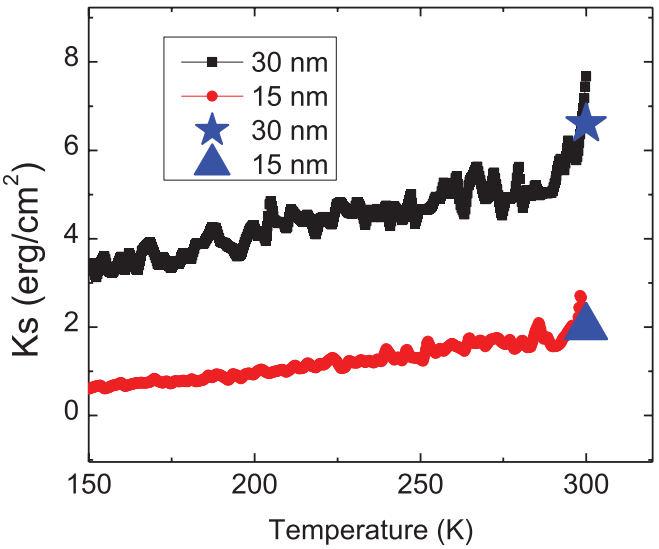

FIG. 6. (Color online) Surface anisotropy constant K_s vs temperature curves calculated from perp. M_s and χ of 30 nm and 15 nm nanobars. Blue star and triangle are the values calculated from M_s and H_s of the corresponding nanobars.

Fig. 4(b), both 15 nm and 30 nm bars show a similar nonzero value, consistent with the thickness *(a)*-independent result in case 1′. From the model, Eqs. (10) and (11), we see that both the saturation field H_s and the ac susceptibility χ depend only on the surface anisotropy and the saturation magnetization M_s. This is a unique phenomenon for single-domain nanobars that allows an accurate determination of the surface anisotropy constant K_s even when the size of the nanobar is still large and the surface anisotropy energy small compared to the bulk contribution. Using Eq. (11), the temperature dependence of the surface anisotropy constant K_s can be calculated from the saturation magnetization M_s and perp. ac susceptibility χ (Fig. 6). The K_s can also be calculated using Eq. (10), from the saturation magnetization M_s and perp. H_s. As shown in the Fig. 6, those data points calculated from Eq. (10) fall right on the K_s curves from Eq. (11).

At the low-temperature end the susceptibility is consistent with cases 3 and 3′. Cases 3 and 3′ predict that the two directions have the same ac susceptibility, Eqs. (8) and (14), which is a function of H_s that increases with H_s. By comparing the experimental curves in Figs. 5(a) and 5(c), we see that the 30 nm bars have a larger saturation field in both directions than the 15 nm bars. Correspondingly, the ac susceptibilities in both directions [Figs. 4(a) and 4(b)] show the predicted trend.

Between these two temperature limits, the broad peak at about 100–150 K indicates the occurrence of a spin reorientation transition. The SRT occurs as the result of the competition between the shape anisotropy and the surface anisotropy, the latter arising from the broken translational symmetry at the surface, via ferromagnetic exchange coupling among neighboring atomic layers.[18] All three anisotropy parameters, K_s, K_1, and K_2, are temperature dependent. K_s normally increases with the temperature and can be found from the saturation field of the initial magnetization curve perpendicular to the bar. The tendency for spins to align along the parallel direction weakens as the temperature is lowered. The spin reorientation from along the length of the bar to the other two directions starts at a temperature below 150 K. The thinner the bar is, the stronger the reorientation, and the larger the peak in the ac susceptibility. As evidenced by Figs. 5(c) and 5(d), the easy axis is strongly along the parallel direction at 300 K, but the parallel and perpendicular directions for the 15 nm bars are almost balanced at 2 K.

IV. SUMMARY

We conducted low-field ac susceptibility measurements on multidomain and single magnetic domain Ni nanostructures (Ni nanobars) arrays. While the thicker nanobars show results consistent with the scaling behavior previously observed in Ni films, thinner nanobars containing only single magnetic domains show a completely quenched ac susceptibility when the ac field is aligned along the long axis of the bars at high temperatures. We identify the magnetic configuration in this case as the "frozen" magnetic moment along this direction. Taking advantage of this identification, we are able to determine the magnetic surface anisotropy energy with cleanly separated energy terms.

ACKNOWLEDGMENTS

This research was conducted at the Center for Nanophase Materials Sciences, which is sponsored at Oak Ridge National Laboratory by the Office of Basic Energy Sciences, US Department of Energy.

APPENDIX: DERIVATION OF INITIAL SUSCEPTIBILITY FOR EACH MAGNETIC CONFIGURATION

Here we consider a single-domain magnetic nanobar of dimension $a \times b \times c$ with $a < b < c$. Because nickel (111) surface has the lowest energy, the nanobar is mainly (111) textured polycrystalline.[9]

In order to derive the magnetic susceptibility, we need first to find the magnetic energy as a function of the moment orientation and the external applied field. The bulk anisotropy energy per unit volume for a cubic lattice is in the form

$$E_b = K_1\left(m_1^2m_2^2 + m_2^2m_3^2 + m_3^2m_1^2\right) + K_2m_1^2m_2^2m_3^2, \qquad \text{(A1)}$$

where m_1, m_2, and m_3 are the components of $\mathbf{m}$ along three crystallographic axes (not to be confused with x, y, and z). The angle θ between $\mathbf{m}$ and the (111) direction (which we choose as the z axis) is given by

$$\cos\theta = \frac{m_1 + m_2 + m_3}{\sqrt{3}}. \qquad \text{(A2)}$$

In order to average over different crystalline orientations, we first choose $(\frac{1}{2}\,\frac{1}{2}\,\bar{1})$ as the x axis, and find the second polar coordinate ϕ by projecting $\mathbf{m} - (\cos\theta/\sqrt{3})(111)$ onto $(\frac{1}{2}\,\frac{1}{2}\,\bar{1})$,

$$\cos\phi = \frac{m_1 + m_2 - 2m_3}{\sqrt{6}}. \qquad \text{(A3)}$$

From these we find

$$m_1 + m_2 = \frac{2}{\sqrt{3}}\cos\theta + \sqrt{\frac{2}{3}}\cos\phi, \tag{A4}$$

$$m_3 = \frac{1}{\sqrt{3}}\cos\theta - \sqrt{\frac{2}{3}}\cos\phi. \tag{A5}$$

Thus,

$$m_1^2 + m_2^2 = 1 - m_3^2 = \frac{1}{3}\sin^2\theta + \frac{2}{3}\sin^2\phi + \frac{2\sqrt{2}}{3}\cos\theta\cos\phi, \tag{A6}$$

$$2m_1m_2 = (m_1+m_2)^2 - m_1^2 - m_2^2 = \frac{5}{3}\cos^2\theta + \frac{4}{3}\cos^2\phi - 1 + \frac{2\sqrt{2}}{3}\cos\theta\cos\phi. \tag{A7}$$

From the last equation, we have

$$m_1^2m_2^2 = \frac{25}{36}\cos^4\theta + \frac{4}{9}\cos^4\phi + \frac{1}{4} + \frac{4}{3}\cos^2\theta\cos^2\phi - \frac{5}{6}\cos^2\theta - \frac{2}{3}\cos^2\phi + \frac{5\sqrt{2}}{9}\cos^3\theta\cos\phi + \frac{4\sqrt{2}}{9}\cos\theta\cos^3\phi - \frac{\sqrt{2}}{3}\cos\theta\cos\phi. \tag{A8}$$

We obtain

$$\left\langle (m_1^2 + m_2^2)m_3^2\right\rangle = \tfrac{1}{6} - \tfrac{1}{3}\cos^2\theta - \tfrac{1}{9}\cos^4\theta, \tag{A9}$$

$$\left\langle m_1^2m_2^2\right\rangle = \tfrac{1}{12} - \tfrac{1}{6}\cos^2\theta + \tfrac{25}{36}\cos^4\theta, \tag{A10}$$

where the angle brackets indicate averaging over ϕ. Thus,

$$\left\langle m_1^2m_2^2 + m_2^2m_3^2 + m_3^2m_1^2\right\rangle = \tfrac{1}{4} - \tfrac{1}{2}\cos^2\theta + \tfrac{7}{12}\cos^4\theta. \tag{A11}$$

We also get

$$\left\langle m_1^2m_2^2m_3^2\right\rangle = \tfrac{1}{108} + \tfrac{1}{12}\cos^2\theta - \tfrac{7}{36}\cos^4\theta + \tfrac{25}{108}\cos^6\theta. \tag{A12}$$

These provide the necessary terms for calculating the average bulk anisotropy for (111) textured polycrystalline solid.

Next, we consider the surface and shape anisotropy. The lowest order surface anisotropy can be written as a surface integral,

$$E_s = \frac{1}{2}K_s\int(\mathbf{m}\cdot\mathbf{n})^2dS, \tag{A13}$$

where $\mathbf{m}$ is the unit vector along the direction of the magnetic moment and $\mathbf{n}$ is the unit vector along the normal of the surface. Now we orient the bar so that a, b, c are the dimensions of the bar along the x, y, z directions, respectively. Integrating E_s, we find

$$E_s = K_s[ab + a(c-b)\sin^2\theta + c(b-a)\sin^2\theta\cos^2\phi], \tag{A14}$$

where θ and ϕ are the usual polar coordinates of the magnetic moment $\mathbf{m}$. If the surface anisotropy favors the moment orientation along the direction with the longest dimension, i.e., the z direction, then it implies that $K_s > 0$.

In order to sum the surface and bulk anisotropy energies together, we orient the (111) direction along the x axis instead of the z axis; thus we need to replace $\cos\theta$ in the bulk anisotropy by $\sin\theta\cos\phi$. The total anisotropy energy per unit volume takes the form

$$E(\theta,\phi) = K_s\frac{c-b}{bc}\sin^2\theta + \left(K_s\frac{b-a}{ab} - \frac{1}{2}K_1 + \frac{1}{12}K_2\right)\sin^2\theta\cos^2\phi + \left(\frac{7}{12}K_1 - \frac{7}{36}K_2\right)\sin^4\theta\cos^4\phi + \frac{25}{108}K_2\sin^6\theta\cos^6\phi. \tag{A15}$$

The orientation of the moment at zero temperature is at the minimum of the total energy per unit volume,

$$F(\theta,\phi) = E(\theta,\phi) - M_sH\cos\theta, \tag{A16}$$

where M_s is the saturation moment per unit volume and H is the magnetic field. Minimizing with respect to θ and ϕ, we find

$$\frac{\partial F(\theta,\phi)}{\partial\theta} = 0 = \left[2K_s\frac{c-b}{bc}\cos\theta + \left(2K_s\frac{b-a}{ab} - K_1 + \frac{1}{6}K_2\right)\cos\theta\cos^2\phi + \left(\frac{7}{3}K_1 - \frac{7}{9}K_2\right)\sin^2\theta\cos\theta\cos^4\phi + \frac{25}{18}K_2\sin^4\theta\cos\theta\cos^6\phi + M_sH\right]\sin\theta, \tag{A17}$$

$$\frac{\partial F(\theta,\phi)}{\partial\phi} = 0 = -\left[2K_s\frac{b-a}{ab} - K_1 + \frac{1}{6}K_2 + \left(\frac{7}{3}K_1 - \frac{7}{9}K_2\right)\sin^2\theta\cos^2\phi + \frac{25}{18}K_2\sin^4\theta\cos^4\phi\right]\sin^2\theta\sin\phi\cos\phi. \tag{A18}$$

For sufficiently large H, the minimum is at $\theta = 0$, i.e., the direction along the magnetic field. For this case, if we neglect the temperature smearing, then $\partial M/\partial H \approx 0$. Additional minima exist if H is less than a saturation field H_s. This possible minima and the corresponding values of $F(\theta,\phi)$ are listed below. Case 1, for $\sin\theta = 0$, which is a minimum if $K_s > 0$,

$$F(\theta,\phi) = F_1 = -M_sH. \tag{A19}$$

This minimum does not have a corresponding saturation field. If we neglect temperature smearing, the initial susceptibility

$\partial M/\partial H \approx 0$. Case 2 is $\cos\phi = 0$ and

$$\cos\theta = -\frac{M_s H bc}{2K_s(c-b)}, \tag{A20}$$

for which we have

$$F(\theta,\phi) = F_2 = K_s\left(\frac{1}{b}-\frac{1}{c}\right) + \frac{M_s^2 H^2 bc}{4K_s(c-b)}. \tag{A21}$$

For F_2 to be a lower energy than F_1, it requires $K_s < 0$. The saturation field is

$$H_s = -\frac{2K_s}{M_s}\left(\frac{1}{b}-\frac{1}{c}\right), \tag{A22}$$

and the initial susceptibility,

$$\frac{\partial M}{\partial H} = -\frac{M_s^2 bc}{2K_s(c-b)}. \tag{A23}$$

Case 3 is $\sin\phi = 0$ and (for small H)

$$\cos\theta \approx -\frac{M_s H}{2K_s\left(\frac{1}{a}-\frac{1}{c}\right)+\frac{4}{3}K_1+\frac{7}{9}K_2}. \tag{A24}$$

This is a minimum if $2K_s(1/a-1/c)+4K_1/3+7K_2/9 < 0$. The corresponding energy is

$$F(\theta,\phi) = F_3 \approx K_s\left(\frac{1}{a}-\frac{1}{c}\right) + \frac{1}{12}K_1 + \frac{13}{108}K_2 + O\left(M_s^2 H^2\right). \tag{A25}$$

For $F_3 < F_1$, it requires $K_s(1/a-1/c)+K_1/12+13K_2/108 < 0$. For $F_3 < F_2$, it requires $K_s(1/a-1/b)+K_1/12+13K_2/108 < 0$. The saturation field is

$$H_s = -\frac{2K_s\left(\frac{1}{a}-\frac{1}{c}\right)-K_1+\frac{1}{6}K_2}{M_s}, \tag{A26}$$

and the initial susceptibility,

$$\frac{\partial M}{\partial H} \approx -\frac{M_s^2}{2K_s\left(\frac{1}{a}-\frac{1}{c}\right)+\frac{4}{3}K_1+\frac{7}{9}K_2}. \tag{A27}$$

The last solution of Eq. (A17) for $\sin\phi = 0$, case 4, is

$$\cos\theta \approx \cos\theta_0 + \frac{M_s H}{4K_s\left(\frac{1}{a}-\frac{1}{c}\right)+\frac{8}{3}K_1+\frac{14}{9}K_2}, \tag{A28}$$

where θ_0 is the angle when $H = 0$ and satisfies

$$2K_s\left(\frac{1}{a}-\frac{1}{c}\right) - K_1 + \frac{1}{6}K_2 + \frac{7}{9}(3K_1-K_2)\sin^2\theta_0 + \frac{25}{18}K_2\sin^4\theta_0 = 0. \tag{A29}$$

To the lowest order in H, the total energy is

$$F(\theta,\phi) = F_4 \approx -\frac{7}{36}(3K_1-K_2)\sin^2\theta_0 - \frac{25}{54}K_2\sin^4\theta_0 - \frac{M_s H}{\cos\theta_0} - \frac{1}{2}M_s H\cos\theta_0. \tag{A30}$$

For this to be a minimum, it requires either $3K_1 > K_2$ or $7K_1+29K_2/9 > 0$. The initial susceptibility is

$$\frac{\partial M}{\partial H} = \frac{M_s^2}{4K_s\left(\frac{1}{a}-\frac{1}{c}\right)+\frac{8}{3}K_1+\frac{14}{9}K_2}. \tag{A31}$$

There are additional minima due to the sixth-order term involving K_2. However, these should usually be higher in energy and will not be considered here.

To calculate the moment and the susceptibility for field perpendicular to the bar (along the b direction), we rotate the coordinate system so that a is along y, b is along z, and c is along x. We have

$$E_s = K_s\left[ab + a(c-b)\cos^2\theta + b(c-a)\sin^2\theta\sin^2\phi\right]. \tag{A32}$$

The anisotropy energy per unit volume is

$$E(\theta,\phi) = -K_s\frac{c-b}{bc}\sin^2\theta + \left(K_s\frac{c-a}{ac}-\frac{1}{2}K_1+\frac{1}{12}K_2\right)\sin^2\theta\sin^2\phi + \left(\frac{7}{12}K_1-\frac{7}{36}K_2\right)\sin^4\theta\sin^4\phi + \frac{25}{108}K_2\sin^6\theta\sin^6\phi. \tag{A33}$$

We are interested in the solutions near $H = 0$, where the solutions should be exactly the same as before except that the axes are rotated and the field-dependent terms are changed.

$$\frac{\partial F(\theta,\phi)}{\partial\theta} = 0 = \left\{-2K_s\frac{c-b}{bc}\cos\theta + \left(2K_s\frac{c-a}{ac}-K_1+\frac{1}{6}K_2\right)\cos\theta\sin^2\phi + \left(\frac{7}{3}K_1-\frac{7}{9}K_2\right)\sin^2\theta\cos\theta\sin^4\phi + \frac{25}{18}K_2\sin^4\theta\cos\theta\sin^6\phi + M_s H\right\}\sin\theta, \tag{A34}$$

$$\frac{\partial F(\theta,\phi)}{\partial\phi} = 0 = \left[2K_s\frac{c-a}{ac}-K_1+\frac{1}{6}K_2 - \left(\frac{7}{3}K_1-\frac{7}{9}K_2\right)\sin^2\theta\sin^2\phi + \frac{25}{18}K_2\sin^4\theta\sin^4\phi\right]\sin^2\theta\sin\phi\cos\phi. \tag{A35}$$

Case 1′, we have $\sin\phi = 0$ and

$$\cos\theta = \frac{M_s H bc}{2K_s(c-b)}. \tag{A36}$$

The saturation field is

$$H_s = \frac{2K_s(c-b)}{M_s bc}, \tag{A37}$$

and the initial susceptibility is

$$\frac{\partial M}{\partial H} = \frac{M_s^2 bc}{2K_s(c-b)}. \tag{A38}$$

Case $2'$ is now the trivial solution of $\sin\theta = 0$ which yields $\partial M/\partial H \approx 0$. Case $3'$ is $\cos\phi = 0$ and

$$\cos\theta \approx -\frac{M_s H}{2K_s\left(\frac{1}{a}-\frac{1}{b}\right)+\frac{4}{3}K_1+\frac{7}{9}K_2}. \tag{A39}$$

The saturation field is

$$H_s = -\frac{2K_s\left(\frac{1}{a}-\frac{1}{b}\right)-K_1+\frac{1}{6}K_2}{M_s}, \tag{A40}$$

and the initial susceptibility is

$$\frac{\partial M}{\partial H} \approx -\frac{M_s^2}{2K_s\left(\frac{1}{a}-\frac{1}{b}\right)+\frac{4}{3}K_1+\frac{7}{9}K_2}. \tag{A41}$$

If $a \ll b$ then the initial susceptibilities along the b and c directions are essentially the same. Case $4'$ is $\sin\theta \approx 1$ and $\sin\phi$ satisfies the equation

$$2K_s\frac{c-a}{ac} - K_1 + \frac{1}{6}K_2 - \left(\frac{7}{3}K_1 - \frac{7}{9}K_2\right)\sin^2\phi + \frac{25}{18}K_2\sin^4\phi = 0. \tag{A42}$$

Then the values for $\cos\theta$ and the initial susceptibility are both the same as in case $1'$.

*gaiz@ornl.gov

[1] A. Enders, R. Skomski, and J. Honolka, J. Phys. Condens. Matter **22**, 433001 (2010).
[2] J. Nogues, J. Sort, V. Langlais, V. Skumryev, S. Surinach, J. S. Munoz, and M. D. Baro, Phys. Rep. **422**, 65 (2005).
[3] J. I. Martin, J. Nogues, Kai Liu, J. L. Vicent, and Ivan K. Schuller, J. Magn. Magn. Mater. **256**, 449 (2003).
[4] H. Takayama, K. Bohnen, and P. Fulde, Phys. Rev. B **14**, 2287 (1976).
[5] B. Heinrich, K. B. Urquhart, A. S. Arrott, J. F. Cochran, K. Myrtle, and S. T. Purcell, Phys. Rev. Lett. **59**, 1756 (1987).
[6] W. Kleemann, J. Rhensius, O. Petracic, J. Ferre, J. P. Jamet, and H. Bernas, Phys. Rev. Lett. **99**, 097203 (2007).
[7] X. H. Song, X. G. Zhang, J. Fan, Y. R. Jin, S. K. Su, and D. L. Zhang, Phys. Rev. B **77**, 092408 (2008).
[8] S. Xiao-Hui and Z. Dian-Lin, Chin. Phys. B **17**, 3495 (2008).
[9] B. Geetha Priyadarshini, S. Aich, and M. Chakraborty, J. Mater. Sci. **46**, 2860 (2010).
[10] Z. Zhang, D. A. Blom, Z. Gai, J. R. Thompson, J. Shen, and S. Dai, J. Am. Chem. Soc. **125**, 7528 (2003).
[11] Z. Gai, J. Y. Howe, J. Guo, D. A. Blom, E. W. Plummer, and J. Shen, Appl. Phys. Lett. **86**, 023107 (2005).
[12] M. A. Marioni, N. Pilet, T. V. Ashworth, R. C. O'Handley, and H. J. Hug, Phys. Rev. Lett. **97**, 027201 (2006).
[13] S. H. Lee, F. Q. Zhu, C. L. Chien, and N. Marković, Phys. Rev. B **77**, 132408 (2008).
[14] R. H. Kodama, S. A. Makhlouf, and A. E. Berkowitz, Phys. Rev. Lett. **79**, 1393 (1997).
[15] C. A. F. Vaz, J. A. C. Bland, and G. Lauhoff, Rep. Prog. Phys. **71**, 056501 (2008).
[16] P. Bruno and J. P. Renard, Appl. Phys. A **49**, 499 (1989).
[17] D. Sander, J. Phys. Condens. Matter **16**, R603 (2004).
[18] X. Hu and Y. Kawazoe, IEEE Trans. Magn. **32**, 4561 (1996).